*Research Article*

# Urban Public Art as the Renewable Energy Hub: Integrating Aesthetics and Functional Design to Create Sustainable Cities

**Yuxia Fu** 🔵

Shijiazhuang Information Engineering Vocational College, China
fuyuxia1990@163.com

**Abstract:** To address the conflict between aesthetic expression and functional efficiency faced by renewable energy facilities in urban spaces, this study proposes a public art installation design framework that integrates interdisciplinary technologies. A multi-source data fusion module integrates geographic context and regional cultural symbols to jointly guide the parametric optimization of device morphology and the layout of energy harvesting components. Complementing this, an improved MPPT (Maximum Power Point Tracking) algorithm—enhanced by a Kalman filter-based dynamic allocation strategy—ensures robust power extraction under the complex irradiance fluctuations induced by the artistic form. Meanwhile, a parametric aesthetic generation algorithm based on genetic algorithm morphological optimization and CycleGAN (Cycle-Consistent Generative Adversarial Network) texture fusion is developed to achieve the dual goals of urban public art as a renewable energy hub. Structural strength verification and interactive experience design ensure safety and public engagement, respectively. Experimental results demonstrate that the proposed scheme achieves a power generation efficiency of 93.4% of the theoretical value under sunny conditions, with a high public satisfaction rate of 85%. A measured annual internal rate of return of 10.6% verifies its environmental and economic benefits. This research provides an innovative paradigm for the synergy between aesthetics and functionality for sustainable urban development.

**Keywords:** *Aesthetic-Functional Synergy; Functional Design; Parametric Generation; Renewable Energy Hub; Urban Public Art*

## 1. Introduction

The construction of urban renewable energy facilities is facing significant aesthetic challenges [1-4]. Although the overall support rate in the EU, the United States, and other regions is generally between 60% and 80% (for example, the support rate for wind power in the UK is over 80%; the public support for community solar energy in the United States is also over two-thirds), in the actual site selection, the public's concerns about the impact on the landscape are particularly prominent [5]. For example, a binary survey in the United States shows that 45% of respondents believe that solar installations affect the aesthetics of the community, while 42% disagree. In historical and cultural blocks or scenic spots, once they enter the key visual range, local resistance often surges. There are also dilemmas at the technical level. In pursuit of aesthetic effects, some studies have proposed designing thin-film photovoltaics into spherical or curved shapes, but this unconventional structure usually results in an efficiency loss of 5-15%, and poor thermal management further accelerates annual performance degradation (0.8-4.9%). Therefore, there is a trade-off between high-density energy output and meeting urban aesthetic needs, which can only reduce efficiency or sacrifice aesthetics [6-8]. For this reason, achieving sustainable urban

transformation requires not only improving technical efficiency but also focusing on project site selection, community engagement, aesthetic design, and maintenance strategies [9-11] to mitigate visual friction and ensure long-term energy benefits. In this context, public art is not only an aesthetic node in urban space but also a multifunctional hub integrating energy harvesting, cultural communication, and citizen interaction. By embedding it into energy infrastructure systems and building a synergistic "art-energy-city" trinity, it is hoped that this transcends the limitations of traditional technology deployment paths and brings about systematic changes in future urban form and energy structure.

In the face of this challenge, Akrofi *et al.* [12] proposed incorporating solar energy considerations into urban planning/design as early as possible to ensure that future cities cannot only use solar energy but also use it to produce energy locally. Catalano *et al.* [13] proposed to solve the problem of biodiversity loss in urban environments through nature-oriented design. This approach focused on the building/city/landscape scale and was supported by emerging digital technologies. Chen's team [14] studied the integration of renewable energy into the architectural field. Zhongshu *et al.* [15] developed public art installations that reflect and celebrate the culture and history of urban areas and promote closer connections between residents and the environment. Chen's team [16] conducted research on a series of smart city quality of life areas in Macau, a tourist destination, and proposed a new concept of "smart city quality of life". These studies have jointly established the strategic position of urban public art as a renewable energy hub.

Existing technical solutions have systemic defects due to disciplinary barriers [17-19]. In the field of morphogenesis, Bhavsar's team [20] focused on the urgent need to optimize the environmental performance of high-density residential areas and provided a replicable framework for creating resilient, energy-efficient, and environmentally sustainable communities. However, this framework did not fully consider the impact of the social and cultural diversity of high-density residential areas on community design. Ajadi *et al.* [21] used simplified calculations and algorithmic calculations as tools to discover the NURBS (Non-Uniform Rational B-Splines) tendencies of mud, providing new low-cost construction opportunities for buildings with irregular flow structures. However, simplified calculations and algorithms may not fully capture the complexity of mud flow, thus affecting the long-term stability of buildings. In the field of energy management, Dolatabadi *et al.* [22] developed a hybrid prediction model based on convolutional neural networks and bidirectional long short-term memory to overcome the risk of high intermittent photovoltaic power generation. However, this hybrid prediction model may rely too much on historical data, resulting in insufficient response capabilities to future emergencies. Shirzadi [23] proposed a mixed integer linear programming method to optimize the daily operating costs of power systems while improving their resilience, including wind turbines, batteries, and traditional power grids. However, the mixed integer linear programming method may lead to excessive computational complexity when dealing with large-scale systems, reducing the efficiency of the system's real-time optimization. In cultural integration technology, Tricarico's team [24] outlined and constructed a conceptual model of cultural and creative enterprises, and proposed policy recommendations for solving the platform space regional development method, but the model failed to deeply consider the sustainable development of cultural and creative enterprises, which may lead to long-term development difficulties. Many studies have pointed out that modularization and integrated optimization often compromise the overall performance of the system: although flexibility and maintainability are improved, the comprehensive efficiency in actual application often cannot reach the ideal state, and is usually far below the theoretical optimal level [25-26]. Although these achievements have promoted the local optimization of urban energy and art facilities, they have not yet formed a collaborative design logic that spans architectural aesthetics, energy scheduling, and cultural expression. As a new urban interface, public art energy devices need to break through disciplinary barriers and build a cross-modal technology integration system at the level of perception structure, control mechanism, and morphological generation.

Based on this, this paper proposes to transform urban public art into a strategic node of energy infrastructure, integrate data-driven morphological generation, aesthetic optimization, and energy control systems, and construct a triple response mechanism of "aesthetics-function-cognition". This path not only improves the quality of urban space at the aesthetic level, but also enhances the responsiveness of urban energy systems to environmental fluctuations at the technical level (resilience), and enhances citizens' understanding and engagement in energy operation mechanisms (energy democratization) through

public visualization devices, providing extra-institutional cultural motivation and perceptual support for sustainable urban development. The core breakthrough of this study lies in the construction of a "technology-humanities" dynamic coupling model. The study draws on the systematic review of 1,682 academic studies on human adaptive response by the Thomas' team [27], and on this basis establishes a geographical and cultural database adapted to regional differences. At the same time, combined with an innovative interactive 3D physical model called "urban pixel" proposed by the Assem's team [28], multiple energy algorithms and texture generators share environmental sensor data, thereby optimizing system performance simultaneously. In terms of interactive systems, referring to the approach proposed by Lee's team [29] to further explore and improve existing methods by leveraging the potential of digital traces, energy scheduling control based on real-time audience behavior data is implemented. The empirical test ultimately achieves a power generation efficiency of 93.4% on sunny days; the cultural symbol recognition rate reaches 4.55 points, and the public satisfaction rate is 85%, verifying the new paradigm of aesthetics empowering technology and energy, reshaping the cultural field.

## 2. Algorithm Design

### 2.1. Construction of Multi-source Data Fusion Module

First, by calling the OpenStreetMap API (Application Programming Interface), the building outline, road network, and terrain elevation data of the target area are extracted to form a geographic spatial feature set $G=\{g_1,g_2,\ldots,g_n\}$, where each $g_i$ represents a multidimensional attribute vector of a geographic element in space. In terms of cultural information collection, based on the local museum database and WordNet semantic extension, a cultural keyword set $C=\{c_1,c_2,\ldots,c_m\}$ is constructed, and a graph database is constructed through entity and attribute relationships to form a cultural semantic network.

To achieve data fusion, the geographic attribute matrix $\mathbf{X}_G \in \mathbb{R}^{n \times d}$ is first reduced in dimension using principal component analysis (PCA), and the covariance matrix is set as:

$$\Sigma = \frac{1}{n}\sum_{i=1}^{n}(\mathbf{x}_i-\bar{\mathbf{x}})(\mathbf{x}_i-\bar{\mathbf{x}})^{\top} \tag{1}$$

$\bar{\mathbf{x}}$ is the mean vector of geographic data. Through eigendecomposition, there is:

$$\Sigma\mathbf{u}_k=\lambda_k\mathbf{u}_k, k=1,2,\ldots,d \tag{2}$$

The first $r$ eigenvectors $\{\mathbf{u}_1,\ldots,\mathbf{u}_r\}$ corresponding to the maximum eigenvalue $\lambda_k$ are selected to form the dimensionality reduction projection matrix $\mathbf{U} \in \mathbb{R}^{d \times r}$, and the dimensionality reduction transformation is completed:

$$\mathbf{Z}_G=\mathbf{X}_G\mathbf{U} \tag{3}$$

$\mathbf{Z}_G \in \mathbb{R}^{n \times r}$ is the geographic feature matrix after dimensionality reduction.

For the cultural keyword set, the TF-IDF (Term Frequency-Inverse Document Frequency) weight matrix $W \in \mathbb{R}^{m \times k}$ is calculated, whose elements are defined by Equation (4) as the weighted frequency of the $j$-th keyword in the $i$-th document:

$$w_{ij}=tf_{ij}\times\log\frac{N}{df_j} \tag{4}$$

$tf_{ij}$ represents the frequency of keyword occurrence; $df_j$ is the number of documents containing the keyword $j$; $N$ is the total number of documents, which enhances the keyword discrimination.

Finally, the reduced-dimensional geographic feature $\mathbf{Z}_G$ and the cultural feature vector $\mathbf{Z}_C$ (obtained by weight matrix mapping) are fused into a unified feature vector:

$$\mathbf{F}=\alpha\cdot\mathbf{Z}_G+(1-\alpha)\cdot\mathbf{Z}_C, \ \alpha\in[0,1] \tag{5}$$

The weight coefficient $\alpha$ adjusts the fusion ratio of geographic and cultural features. The fused feature is imported into the Grasshopper platform through the Python-Rhino interface to control the NURBS curve control points and achieve parametric generation of the basic form of the device. The fused feature vector is not only used for morphological modeling but also serves as the basic input for the subsequent energy harvesting subsystem and aesthetic expression algorithm, realizing the full-process

embedding of geographic and cultural adaptability, so that the subsequent module design has a unified data starting point and semantic coherence, forming the first collaborative interface. The fused feature vector *F* undergoes further normalization and quantization to generate two parameter sets: one for engineering optimization (e.g., MPPT gain coefficients, Kalman filter initial covariance) and another for aesthetic generation (e.g., initial population distribution for the genetic algorithm, style weights for CycleGAN). For instance, the density index of the cultural semantic network is mapped to the observation noise adjustment coefficient of the Kalman filter, while the mean curvature of geographic spatial features is converted into the structural preservation loss weight $\lambda_{str}$ in CycleGAN. This mapping mechanism ensures that geographic and cultural data influence not only morphological design but also enable closed-loop optimization in system control and aesthetic expression. The overall system design process is shown in Figure 1.
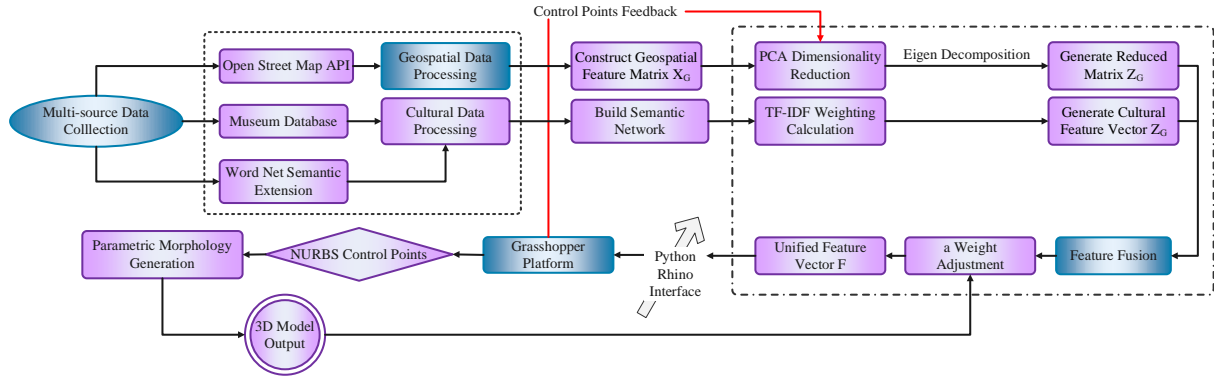


**Figure 1.** Schematic diagram of the overall system design process

## 2.2. Optimization of Energy Harvesting Subsystem

The photovoltaic module parameters are established based on the Sandia photovoltaic model. Its current-voltage characteristic curve is described by the following equation:

$$I = I_{\mathrm{ph}} - I_0 \left[ \exp\left( \frac{q(V+IR_s)}{nkT} \right) - 1 \right] - \frac{V+IR_s}{R_{\mathrm{sh}}} \tag{6}$$

$I$ and $V$ are the photovoltaic module current and voltage, respectively; $I_{\mathrm{ph}}$ is the photocurrent; $I_0$ is the reverse saturation current; $q$ is the electron charge; $n$ is the ideal factor of the diode; $k$ is the Boltzmann constant; $T$ is the junction temperature; $R_s$ and $R_{\mathrm{sh}}$ are the series and parallel resistances, respectively.

To improve the efficiency of maximum power point tracking (MPPT), the improved incremental admittance method is adopted. The current disturbance prediction term $\Delta I_{\mathrm{pred}}$ is applied, and the maximum power point condition is modified as follows:

$$\frac{dP}{dV} = I + V \frac{dI}{dV} + \Delta I_{\mathrm{pred}} \approx 0 \tag{7}$$

The disturbance prediction is calculated based on the current and historical changes, which effectively suppresses oscillations and accelerates convergence.

The power prediction module establishes a second-order state space model, which is expressed as:

$$\begin{cases} \mathbf{x}_{k+1} = A\mathbf{x}_k + B\mathbf{u}_k + \mathbf{w}_k, \\ \quad \mathbf{y}_k = C\mathbf{x}_k + \mathbf{v}_k, \end{cases} \tag{8}$$

The state vector $\mathbf{x}_k$ contains the power output and environmental disturbance variables, and the input $\mathbf{u}_k$ is the collected wind speed and light intensity. The process noise $\mathbf{w}_k$ and measurement noise $\mathbf{v}_k$ obey zero-mean Gaussian distribution, respectively. Recursive Least Squares (RLS) is used to estimate parameters in real-time to ensure that the model can dynamically adapt to environmental changes.

The filter stage is extremely important for the art-form device proposed because of its sculptural morphology that creates time-varying shading patterns, resulting in high-frequency irradiance fluctuation (on-site testing has validated the presence of high-frequency fluctuating irradiance). By not estimating

states, the fluctuations in irradiance would be considered an actual change in MPPT which results in negative consequences for the device.

Sensor data is fused through the Extended Kalman Filter (EKF), and the nonlinear state update and observation equations are:

$$\mathbf{x}_{k+1}=f(\mathbf{x}_k,\mathbf{u}_k)+\mathbf{w}_k, \quad \mathbf{y}_k=\mathrm{h}(\mathbf{x}_k)+\mathbf{v}_k \tag{9}$$

The filtering process relies on the linearized states of the Jacobian matrices $\mathbf{F}_k=\frac{\partial f}{\partial \mathbf{x}}|_{\hat{\mathbf{x}}_k|k-1}$ and $\mathbf{H}_k=\frac{\partial \mathrm{h}}{\partial \mathbf{x}}|_{\hat{\mathbf{x}}_k|k-1}$, and dynamically corrects the state estimation to ensure the accuracy of multi-source data fusion and the stable operation of the system. In addition, the wind speed and light parameters processed by the filter are synchronously transmitted to the aesthetic algorithm module and the interactive system, driving the visual feedback mechanism while maintaining the stability of energy scheduling, and realizing the cross-module information coordination of "environment-energy-aesthetics". Additionally, in real-time, geo-cultural parameters from the fusion module are sent to the MPPT and Kalman filter, allowing both devices to change their settings for optimal filtering, tracking output fluctuations, and improving accuracy of the predicted outputs. When the cultural semantic network recognizes a "historically preserved area", the MPPT reduces the perturbation step size in order to have a smoother output; when the geographic features signal that the area is an "open area", the Kalman filter lowers its observation noise covariance for better predictions. Through the use of the parametric linkage method, both the Engineering System and Cultural Semantic Network will adaptively respond to geographic and cultural contexts. The key parameter settings are shown in Table 1.

**Table 1.** Key parameter settings

| Parameter Description | Symbol | Value | Unit |
|---|---|---|---|
| Photogenerated current | $I_{ph}$ | 5.32 | A |
| Reverse saturation current | $I_0$ | $1.1 \times 10^{-10}$ | A |
| Series resistance | $R_s$ | 0.28 | $\Omega$ |
| Shunt resistance | $R_{sh}$ | 460 | $\Omega$ |
| Diode ideality factor | n | 1.25 | — |
| Junction temperature | T | 318.15 | K |
| Current disturbance prediction | $\Delta I_{pred}$ | ±0.06 | A |
| State transition matrix | A | $\begin{bmatrix} 1 & 0.1 \\ 0 & 0.95 \end{bmatrix}$ | — |

To accurately quantify the optical loss introduced by the aesthetic coating, this study conducted systematic spectral characteristic tests on the screen-printed colored coating. Based on data measured by a spectrophotometer, the average light transmittance of the coating within the photovoltaic response spectrum range (400–1100 nm) is 92.5%. The corresponding optical loss coefficient is defined as: $Optical\ loss\ coefficient = 1 - Average\ transmittance$. The loss in performance of photovoltaic systems has been addressed by increasing efficiency in terms of light absorption; specifically, the photoelectric conversion efficiency term used within the Sandia photovoltaic system model was modified using a coating transmittance correction factor so that calculated theoretical performance may mimic actual physical/optical limits of the solar cell device type.

### 2.3. Aesthetic Expression Generation Algorithm

Cultural symbols are encoded as words using semantic vectors through embedding models like Word2Vec; this process calculates their cosine similarity with pre-set aesthetic styles (such as "stream-lined", "geometric", "biomimetic") and these numbers are used as cultural fitness M values in the genetic algorithm weight coefficients for these models. Geographic attributes such as curvature, slope and visual corridors are converted into normalised parameters between 0 and 1 to provide a method of controlling the strength/degree of style transfer and colour saturation during texture fusion in CycleGANs. For example; when looking at highly curved areas, their textures receive more emphasis (higher texture fusion weights) due to their strong visual attractiveness; however, historical districts generally receive less emphasis (low colour saturation) since they are considered to be culturally restrained. Morphological generation is represented by B-spline curves, which are defined by control points $\{\mathbf{P}_i\}_{i=0}^{n}$ and basis functions $N_{i,k}(t)$ in the parameter region $t \in [0,1]$:

$$\mathbf{C}(t)=\sum_{i=0}^{n} N_{i,k}(t)\mathbf{P}_i$$

$$\text{Among them } N_{i,1}(t)=\begin{cases} 1, & t_i \leq t < t_{i+1} \\ 0, & \text{Other} \end{cases}, N_{i,k}(t)=\frac{t-t_i}{t_{i+k-1}-t_i} N_{i,k-1}(t)+\frac{t_{i+k}-t}{t_{i+k}-t_{i+1}} N_{i+1,k-1}(t).$$

(10)

In the genetic algorithm, a comprehensive fitness function $F$ is defined, combining the device projection area $A$, curvature continuity index $S$, and cultural feature fit $M$:

$$F=w_1 \frac{A}{A_{max}} + w_2 \left(1-\frac{\int_0^1 |\kappa'(t)|\,dt}{S_{max}}\right) + w_3 \frac{M}{M_{max}}$$

(11)

The weight $w_1$ satisfies $\sum_i w_i=1$, and the curvature change rate $\kappa'(t)$ measures the smoothness of the curve. The three together guide the morphological optimization to take into account both structural aesthetics and semantic expression.

Texture fusion is based on the CycleGAN framework, and the training objective function includes the generation adversarial loss $L_{GAN}$, cycle consistency loss $L_{cyc}$, and structure preservation loss $L_{str}$:

$$L=L_{GAN}(G,D_X,Y)+L_{GAN}(F,D_Y,X)+\lambda_{cyc}L_{cyc}(G,F)+\lambda_{str}L_{str}(G)$$

(12)

$$L_{str}(G)=E_{x\sim P_{data}(x)}\left[\|\phi(x)-\phi(G(x))\|^2\right]$$

(13)

$\phi$ represents the structural features extracted from the pre-trained network, which is used to maintain the consistency of local details and global structure of the texture mapping.

The final parameters are passed in real-time by calling the Rhino API through Grasshopper, achieving a high degree of integration of morphology, color, and texture, significantly improving the visual appeal and cultural recognition of the device. To achieve seamless fusion of aesthetic texture with photovoltaic functionality, this study employs screen-printed colored photovoltaic glass coating technology as the physical medium. First, the two-dimensional texture image generated by CycleGAN is converted into a translucent color block distribution map, where each color block corresponds to a specific screen-printing ink formulation to ensure color fidelity. This coating is precisely printed on the back surface of the photovoltaic glass, forming a laminated structure that avoids external wear and contamination. The coating thickness is controlled at 15–20 micrometers to balance color saturation and light transmittance. This process ensures visual expression of the texture while minimizing blocking and scattering of incident light. The cultural characteristics embedded in texture generation are derived from the output of the fusion module in Section 2.1. The geometric morphology must be compatible with the safety thresholds of the structural parameters in Section 2.4, thus forming a two-way constraint between aesthetic design and structural performance. This process, which enables the simultaneous control of morphology, structure, and texture parameters on the Rhino platform, is the core of system collaboration. The morphology generation process is shown in Figure 2.
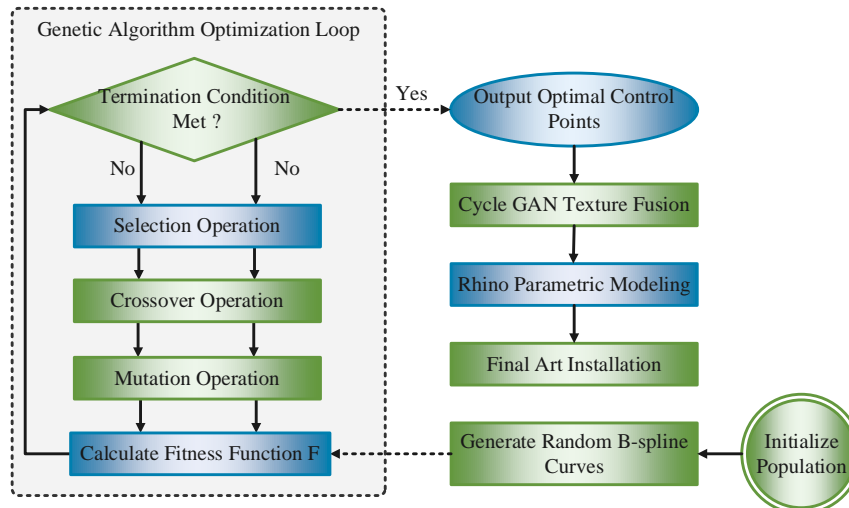


**Figure 2.** Schematic diagram of the morphology generation process

### 2.4. Structural Strength Verification Method

After the three-dimensional model of the device is imported, the TetGen tool is used to generate tetrahedral elements based on the curvature-driven adaptive mesh strategy to meet the meshing requirements of dense distribution in high curvature areas. The material properties adopt the anisotropic elastic-plastic constitutive model, and the stress-strain relationship is defined as:

$$\sigma = \mathbf{D}:(\varepsilon - \varepsilon^p) \tag{14}$$

$\sigma$ is the stress tensor; $\varepsilon$ is the total strain tensor; $\varepsilon^p$ is the plastic strain part; $\mathbf{D}$ is the elastic stiffness matrix of the anisotropic material. This model can characterize the nonlinear response of composite materials under multiaxial loading.

Static analysis is implemented using ANSYS APDL. After applying boundary conditions such as deadweight, wind pressure, and fixed support, the node displacement $\mathbf{u}$ must satisfy the linear system:

$$\mathbf{Ku} = \mathbf{F} \tag{15}$$

$\mathbf{K}$ is the global stiffness matrix, and $\mathbf{F}$ is the load vector. The principal stress trajectory obtained after the solution is used for subsequent fatigue evaluation.

The fatigue life calculation adopts the Goodman correction model, which is expressed as follows:

$$\frac{\sigma_a}{\sigma_e} + \frac{\sigma_m}{\sigma_u} \leq 1 \tag{16}$$

$\sigma_a$ is the stress amplitude; $\sigma_m$ is the average stress; $\sigma_e$ is the material fatigue limit; $\sigma_u$ is the ultimate tensile strength. If the inequality is satisfied, the structure is considered safe. Otherwise, the feedback mechanism is triggered to automatically adjust the control point layout in the parameterized model, thereby achieving the linkage optimization of structural performance and aesthetics. When a high stress risk area is identified in the structural analysis, the system automatically triggers the feedback adjustment of the aesthetic generation module, and by modifying the local curvature or control point layout, a collaborative closed-loop of design intent and engineering safety is achieved. This feedback mechanism and Section 2.3 jointly construct a "strength-morphology" two-way linkage strategy to ensure overall stability while maintaining visual expression. The material mechanical parameters are shown in Table 2.

**Table 2.** Material mechanical parameters

| Parameter Description | Symbol | Value | Unit | Note |
|---|---|---|---|---|
| Fatigue strength limit | $\sigma_e$ | 260 | MPa | Used in Goodman criterion (Eq. 16) |
| Ultimate tensile strength | $\sigma_u$ | 680 | MPa | Used in Goodman criterion (Eq. 16) |
| Plastic strain tensor | $\varepsilon^p$ | – | – | Internal variable in Eq. (14), simulation-defined |
| Elastic stiffness matrix | D | – | – | Constitutive matrix for anisotropic model |
| Load vector | F | – | N | External load including self-weight, wind |
| Global stiffness matrix | K | – | – | Computed by FEM (Finite Element Method) software (Eq. 15) |

To facilitate the direct experience of public participation, we have created an in-person interactive element: a 27-inch weather-resistant display positioned at a comfortable height and providing several layers of current data(i) instantaneous power generation (KW) and total $CO_2$ reductions (kg); indicated by a vertical animation of a "green leaf" that gets larger as more energy is produced; (ii) a representative map of the community which labels other installations of peers, as well as where people can share energy with. It provides an opportunity for participants to have a unique factor (such as "Solar Guardian #247") to identify themselves by receiving a personalized badge after they have interacted for more than thirty seconds. At the same time, the LED array that surrounds the sculpture will respond to the proximity of the participant and/or gestures. The closer the participants is to the sculpture (<2m) the brighter the base light will become. The light emitted from the bottom of the curved element will produce a rippling effect of cyan when the participant "waves" their hand within a certain distance (as determined by the ultrasonic array) at the top of the curved section. The combination of these sensory experiences allows participants to receive rapidly changing information about energy sources and effectively creates a tangible way to participate in the process of "Energy Democratization."

### 2.5. Interactive Experience Integrated Design

Infrared pyroelectric and ultrasonic sensor arrays are arranged around the device to obtain the direction and relative distance information of the audience, respectively. The exponentially weighted

moving average (EWMA) method is used to filter the measurement value to reduce the transient interference signal in the multi-source data. The filter output is:

$$\hat{d}_t = \alpha \cdot d_t + (1-\alpha) \cdot \hat{d}_{t-1}, \quad \alpha \in (0,1) \tag{17}$$

$\hat{d}_t$ is the current filtered distance estimate; $d_t$ is the original sensor measurement value; $\alpha$ controls the response speed and smoothness.

The local edge computing module uses an STM32 microcontroller and deploys a LightGBM (Light Gradient Boosting Machine) classification model that has been optimized by pruning and quantization. For each frame of sensor feature $\mathbf{x}=[\Delta d, \theta, v, t]$, the corresponding behavior category $y \in \{Close, \text{Stop}, \text{Leave}\}$ is predicted. The prediction function is:

$$\hat{y} = \arg\max_c \sum_{k=1}^{K} \gamma_k \cdot h_k(\mathbf{x}) \tag{18}$$

$h_k$ represents the $k$-th regression tree, and $\gamma_k$ is its learning rate. The model improves the classification stability and real-time performance through weighted integration. The recognition result is sent to the main control logic unit through the DMA (Direct Memory Access) module to trigger the device feedback response.

In the visual feedback path, the PWM (Pulse Width Modulation) controller drives the WS2812 LED (Light Emitting Diode) array, mapping different dynamic color schemes based on the audience's behavior category. The color state $\mathbf{C}_t = [R_t, G_t, B_t]$ is controlled by a three-segment function:

$$C_{i,t} = \begin{cases} min(255, k_i \cdot d_t), & y=Close \\ a_i \cdot \sin(\omega t + \phi_i) + b_i, & y=\text{Stop} \quad i \in \{R, G, B\} \\ max(0, 255 - k_i \cdot d_t), & y=\text{Leave} \end{cases} \tag{19}$$

$d_t$ is the current distance, and $k_i$, $a_i$, $b_i$, and $\phi_i$ are the response control parameters, ensuring that the feedback color is both rhythmic and perceptible. All status data are synchronized to the local server and pushed to the mobile terminal via the MQTT (Message Queuing Telemetry Transport) protocol, building a closed-loop of remote monitoring, data visualization, and user interaction. The behavior recognition module not only triggers LED feedback but also uploads user behavior feature data to the local server, driving the subsequent morphological adjustment and texture migration model update training, thereby realizing the iterative mechanism of "interactive feedback design" and building a complete closed-loop of technology-humanity collaboration. The interactive system module architecture is shown in Figure 3.
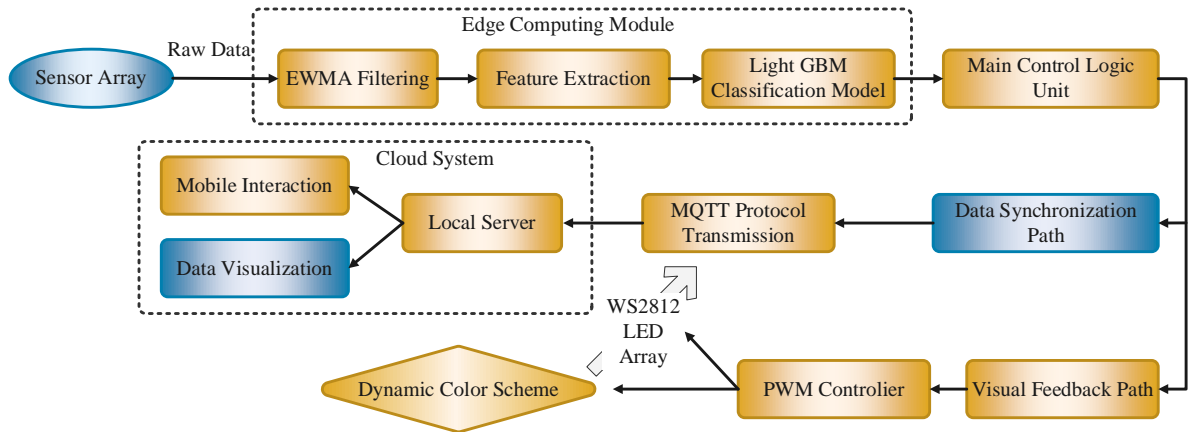


**Figure 3.** Interactive system module architecture

## 2.6. Urban Energy Network Integration

To strengthen the "hub" function of urban public art installations within the energy system, this study further applies an urban energy network integration mechanism, enabling the installations to function as microgrid nodes and actively participate in local energy scheduling and sharing. At the hardware connectivity layer, the installations integrate Zigbee and LoRa dual-channel communication modules to achieve low-power wide area network connectivity with surrounding renewable energy

facilities. Data is synchronized with the city's main grid dispatching platform via edge computing nodes, enabling autonomous convergence, diversion, and storage regulation.

The system utilizes an energy priority allocation algorithm to dynamically schedule the output of wind, solar, and energy storage units. Based on a time-of-day load demand forecasting model and device status awareness, this algorithm prioritizes resources based on power generation efficiency, response speed, and storage capacity. Highly responsive devices are prioritized during peak sunlight hours; less efficient but stable output sources are used for nighttime compensation; energy storage devices serve as emergency backup units to respond to sudden demand. The integrated architecture of the urban public art energy hub network is shown in Figure 4.
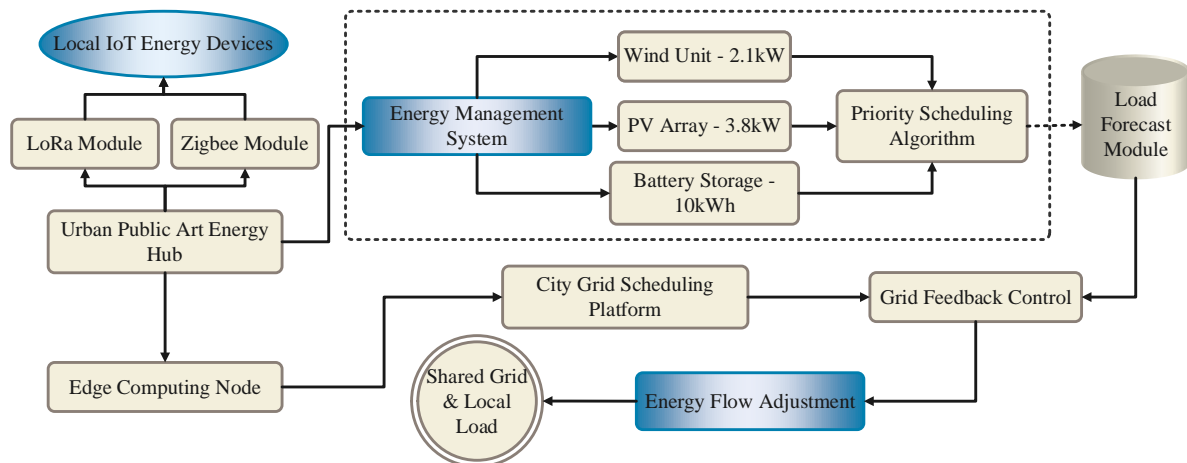


**Figure 4.** Integrated architecture of the urban public art energy hub network

## 3. Experimentation and Verification

### 3.1. Overall Device Performance Testing

This experiment constructs a wind-solar hybrid power generation device equipped with photovoltaic and wind power generation systems, combined with an MPPT controller and a bidirectional DC-DC (Direct Current to Direct Current) converter, to conduct comprehensive performance testing. The system uses parallel data acquisition modules to monitor environmental parameters (such as sunlight and wind speed) and power generation data in real-time, ensuring the accuracy of various sensors and the synchronization of control signals. Under various weather conditions, the device's startup threshold, power fluctuations, and energy distribution are recorded to provide data support for optimizing power generation efficiency and scheduling strategies. Relevant experimental conditions and environmental parameters are shown in Table 3.

**Table 3.** Experimental conditions and environmental parameters

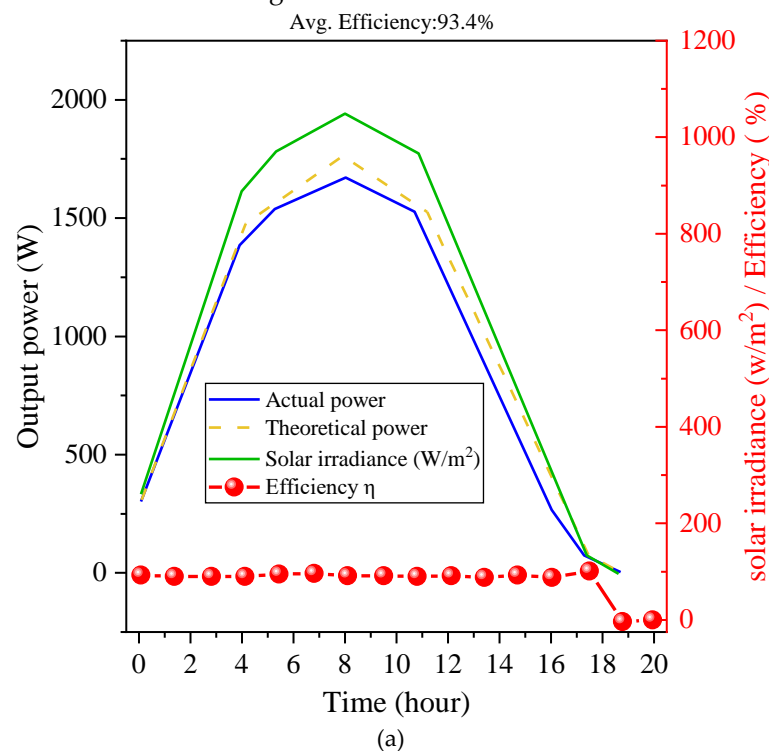| Parameter | Value Range | Unit | Notes |
|---|---|---|---|
| Average Solar Irradiance | 650–920 | W/m² | Measured via DHT22 and cross-validated with calibrated meter |
| Average Wind Speed | 2.8–6.4 | m/s | Based on the GM8908 sensor, valid for small turbine activation |
| Ambient Temperature | 18–34 | °C | Daily variation, typical of urban summer conditions |
| Relative Humidity | 42–70 | % | Measured concurrently with temperature |
| Light Sensor Error (vs standard) | ±3.2 | % | Verified by regression against the reference instrument |
| Wind Sensor Error (vs standard) | ±3.8 | % | Within acceptable urban measurement tolerance |
| Data Sampling Frequency | 1 | Hz | Real-time logging to SD card via STM32 |
| Voltage Measurement Accuracy | ±1.5 | % | Based on INA226 ADC(Analog-to-Digital Converter) specifications |
| Power Generation Test Duration | 12 | months | Full diurnal cycles with varying weather |
| MPPT Controller Response Delay | ≤85 | ms | Evaluated via logic analyzer |
| Signal Synchronization Rate | ≥95 | % | Across subsystems (MPPT, sensors, DC-DC converter) |

The experimental conditions and environmental parameters in Table 3 detail the operating conditions of the wind-solar hybrid power generation system in a typical urban summer environment. Average solar irradiance ranges from 650 to 920 watts per square meter, indicating that the system operates under medium-to-high light intensities. The DHT22 light sensor exhibits a ±3.2% error compared to a calibrated light meter, ensuring the reliability of the light data. Wind speeds range from 2.8 to 6.4 meters per second, suitable for the startup and stable operation of small horizontal-axis wind turbines. The GM8908 wind

speed sensor maintains an error of ±3.8%, meeting the requirements for urban microclimate measurement. Ambient temperature and relative humidity range from 18 to 34 degrees Celsius and 42 to 70%, respectively, simulating the thermal and humid fluctuations experienced in a real urban summer. The data sampling frequency is 1 Hz, and the voltage measurement error is ±1.5%, ensuring the timeliness and accuracy of the collected data. Twelve months of continuous testing cover all weather conditions, recording the system's startup threshold, power fluctuations, and energy distribution, providing comprehensive data for power generation efficiency and scheduling optimization. The controller response delay is within 85 milliseconds, and the signal synchronization rate is no less than 95%, ensuring efficient and stable coordination of system commands.

## 3.2. Power Generation Efficiency Indicators

All-day sampling tests are conducted under representative sunny, cloudy, and breezy weather conditions, and the actual output power of the PV (photovoltaic) panels and wind turbine is recorded. Using the configured INA226 current/voltage acquisition module, power data for each channel is measured at a 1 Hz frequency, and light intensity (W/m²) and wind speed (m/s) are recorded synchronously with environmental sensors. The Sandia photovoltaic model determines the theoretical maximum efficiency that can be achieved with a curved surface based on an actual 3D configuration taking into effect the environmental conditions (solar insolation and temperature). The theoretical maximum efficiency does not include any aesthetic considerations such as texture-induced losses or shading by adjacent structures, and assumes that maximum power point tracking (MPPT) is being done perfectly. The theoretical maximum efficiency is based upon the upper limit for this type of photovoltaic surface; it is not a reference for a flat panel. For wind energy predictions, the Betz limit is used and adjusted for the actual area of the integrated turbine.

The actual and theoretical power generation is accumulated in hourly time windows. A proportional function is used to calculate the full-day power generation efficiency, eliminating errors during system initial startup and the low-threshold power range. The test results are compared over multiple days to analyze the power generation performance response curves under different weather conditions, with a focus on the impact of MPPT control on power generation efficiency under different weather conditions. A comparison of the power generation performance of the urban renewable energy art installation under different weather conditions is shown in Figure 5.
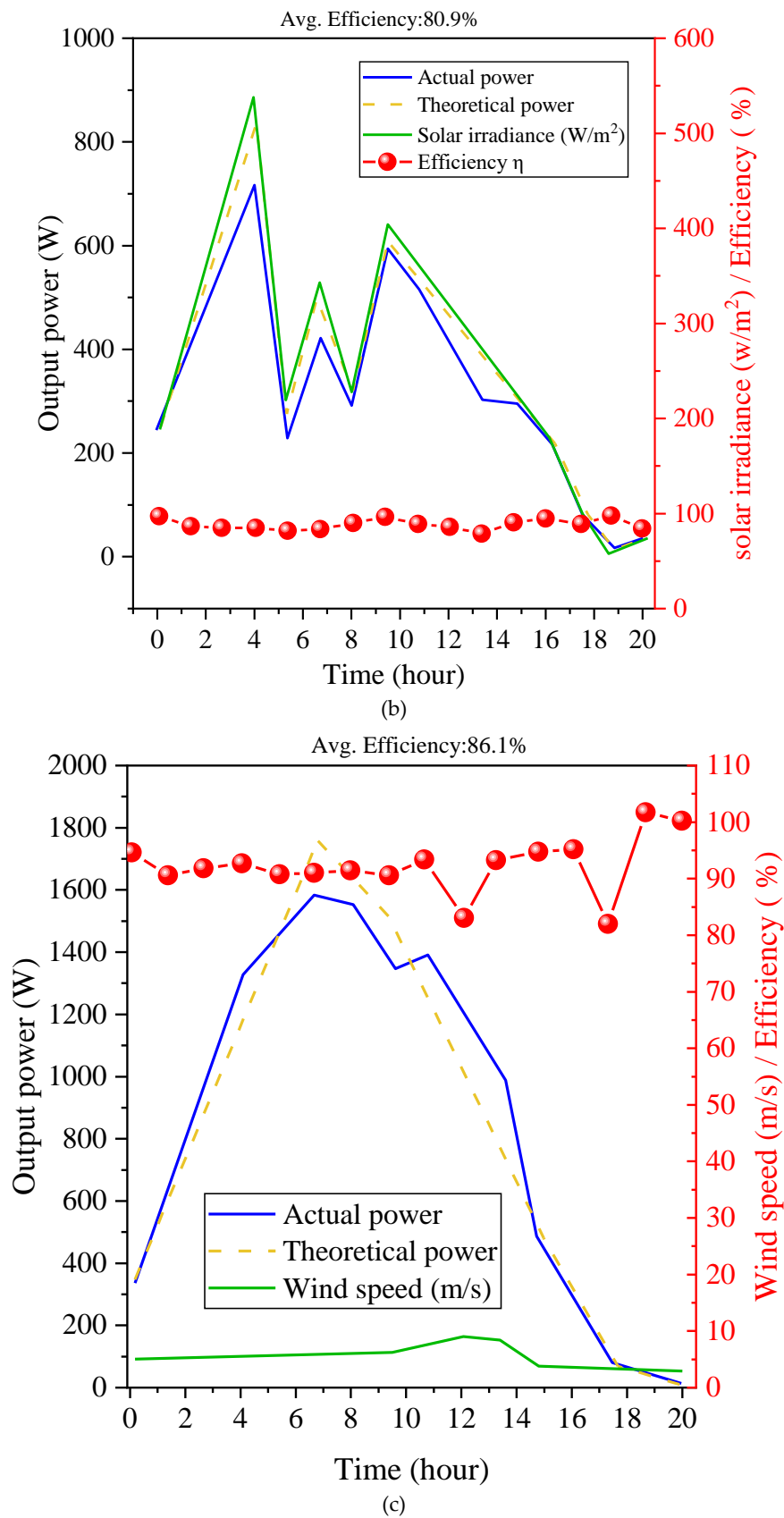


(a)

(b)



(c)

**Figure 5.** Comparison of the power generation performance of the urban renewable energy art installation under different weather conditions; Sub-Figure (a). Power generation efficiency and solar irradiance response curve under sunny conditions, Sub-Figure (b). Power generation efficiency and solar irradiance response curve under a cloudy day, Sub-Figure (c). Power generation efficiency and wind energy response curve under breezy day

Figure 5 shows the power generation performance response curves of the urban renewable energy art installation under three weather conditions: sunny, cloudy, and breezy. In Sub-Figure A, the theoretical

power reaches a maximum of approximately 1765W at 11:00 AM, with an actual power peak of 1675W and an average efficiency of 93.4%. The output power curve exhibits a stable bell shape, well matching the light intensity and theoretical values. This demonstrates high MPPT control accuracy and timely PV module response under sunny conditions. Sub-Figure B, reflecting cloudy conditions, shows a significant drop in theoretical output, with significant fluctuations. The maximum output is approximately 847W, while the actual power is only around 728W, with an average efficiency of 80.9%. The dramatic fluctuations in power output are caused by the constant light intensity between 0 and 550 W/m² throughout the day. Sub-Figure C shows the wind power generation response under breezy conditions. The actual peak power is approximately 1585W, slightly lower than the theoretical value of 1761W, with an efficiency of 86.1%. The green curve shows wind speeds remain between 1.8 and 8.1 m/s throughout the day, indicating that output is primarily limited by low wind speed input, while the overall response is more stable than under cloudy conditions. MPPT tracking performance are shown in Figure 6.
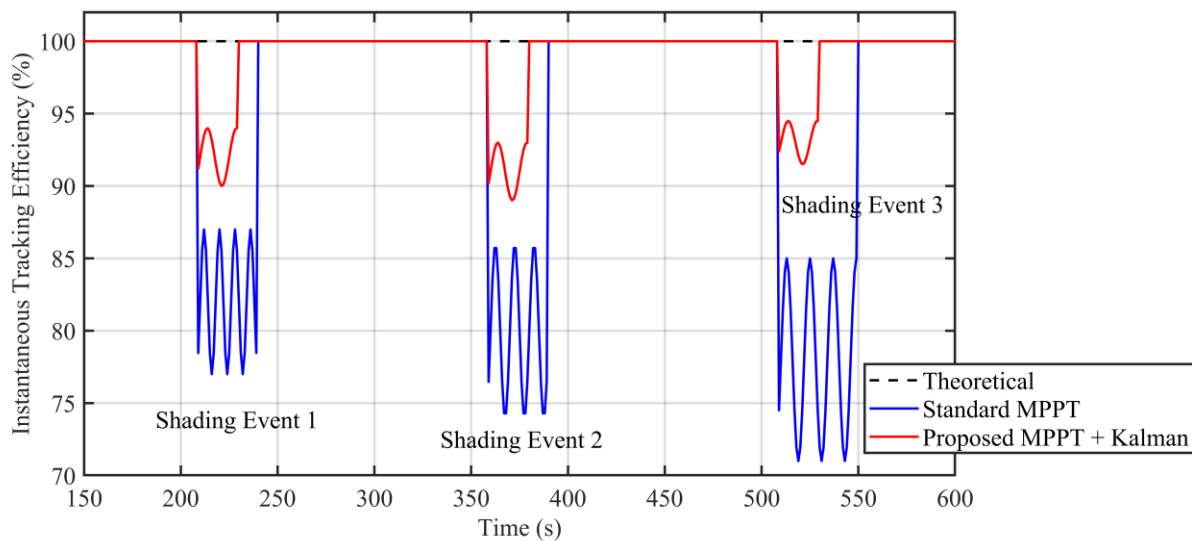


**Figure 6.** MPPT tracking performance under dynamic self-shading

To further validate the necessity of Kalman-enhanced MPPT for artistic morphologies, we conducted a controlled shading experiment simulating the dynamic self-occlusion arising from the sculpture's own geometry. Under three shading events, the standard method exhibited persistent oscillation and slow recovery, whereas the proposed MPPT+Kalman scheme maintained stable tracking with significantly reduced ripple. This confirms that the Kalman filter effectively decouples true environmental dynamics from high-frequency shading-induced noise, ensuring robust power extraction without compromising aesthetic form.

### 3.3. Public Aesthetic Acceptance

During the formal testing phase, 100 residents and visitors with basic aesthetic judgment skills near the design implementation area are selected as respondents to conduct a dual public aesthetic and behavioral evaluation. First, a five-point rating scale is used, encompassing five evaluation dimensions: form harmony, color integration, cultural identity, visual appeal, and overall aesthetics. Each dimension is scored item by item. The questionnaire is completed via a tablet, and the data is synchronized to a database in real-time. Second, to evaluate the actual impact of public behavior on energy system operation, Bluetooth beacons and WiFi probe modules are deployed at the installation site to track the frequency and duration of users viewing the energy visualization interface in the App and record any interactions with the dispatch system.

By collecting valid behavioral data samples over a twelve-month period, the frequency of users actively accessing the energy consumption interface or triggering feedback animations during their average viewing time is calculated. The "influence rate of public behavior on energy dispatch" is defined as the proportion of participating user behaviors that trigger a system response.
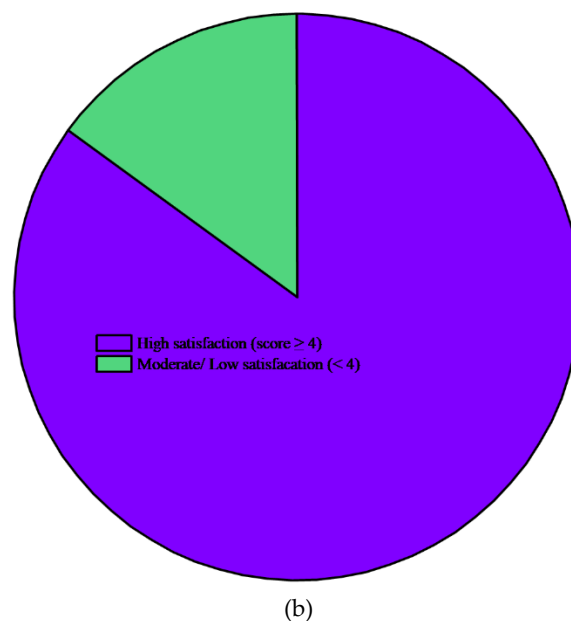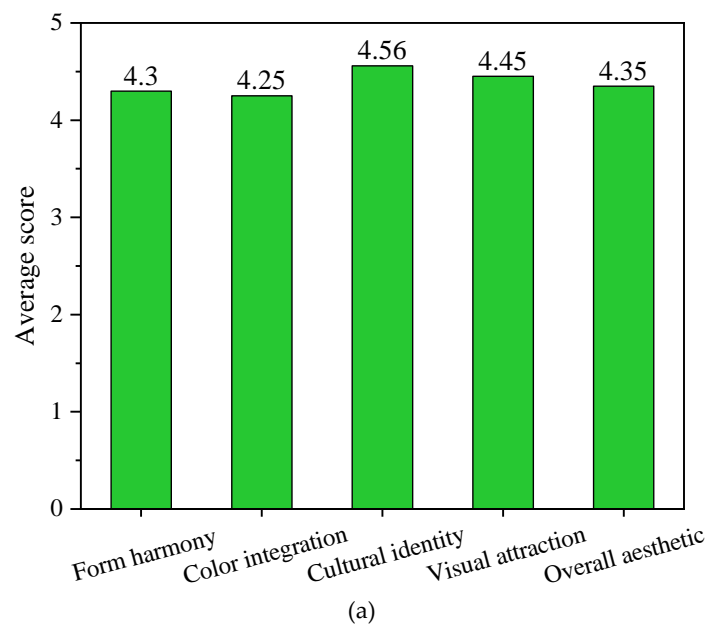
In addition, oral interviews are conducted with samples whose scores deviate significantly from the median to identify evaluation blind spots and provide feedback suggestions, further refining the system

design logic. To enhance the rigor of aesthetic evaluation, this study adopts a combined approach of quantitative design metrics and user perception research. At the morphological level, "curvature continuity index" and "color harmony index" are introduced as objective evaluation criteria; at the perceptual level, eye-tracking experiments capture user gaze hotspots and dwell times, cross-validated with five-dimensional Likert scale ratings. Ultimately, aesthetic scores, cultural symbol recognition rates, and interaction behavior frequencies constitute a multidimensional evaluation system, ensuring systematic and repeatable assessment. Table 4 has been added to present the correlation analysis between various dimensional metrics and user satisfaction.

**Table 4.** Quantitative aesthetic evaluation metrics and user perception correlation analysis

| Parameter Description | Quantitative Metric | Measurement Method | Correlation with User Satisfaction |
|---|---|---|---|
| Form Harmony | Curvature Continuity Index | Geometric Analysis | 0.72 |
| Color Integration | Color Harmony Index | Std. Dev. in Lab Color Space | 0.68 |
| Cultural Identity | Semantic Similarity Score | Word Embedding Model Calculation | 0.81 |
| Visual Appeal | Gaze Hotspot Density | Eye-tracking | 0.75 |
| Overall Aesthetic Feeling | Comprehensive Perception Score | 5-point Scale Average | 0.88 |

The results of the public aesthetic and behavioral analysis are shown in Figure 7.
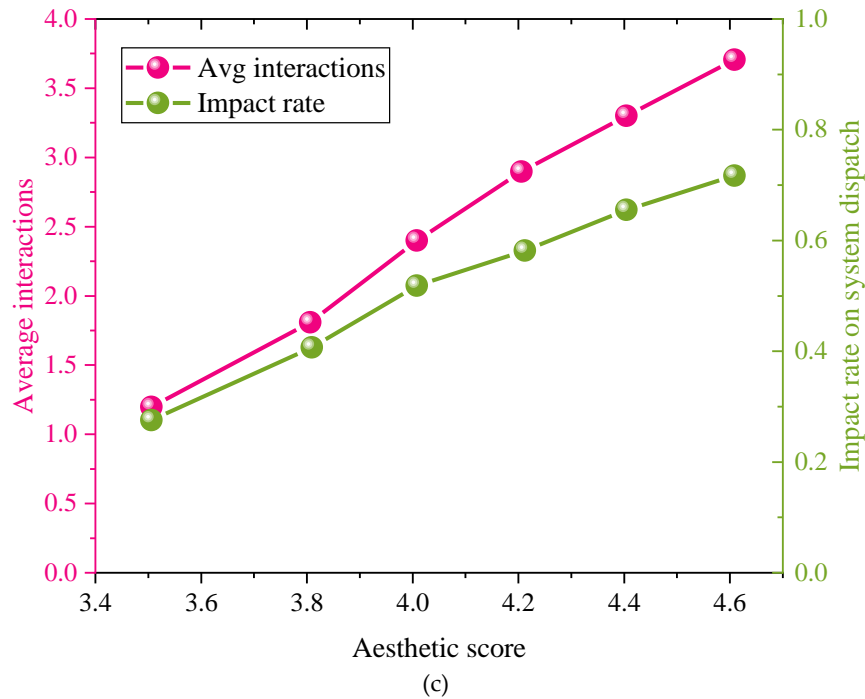


(a)



(b)

(c)

**Figure 7.** Analysis of public aesthetic acceptance; Sub-Figure (a). Aesthetic rating distribution, Sub-Figure (b). Satisfaction feedback percentage, Sub-Figure (c). Impact of public behavior on system scheduling

Figure 7 shows the public's acceptance and behavioral feedback on renewable energy public art installations that integrate aesthetics and functional design. Sub-Figure A shows that, among the five aesthetic evaluation dimensions, cultural identity scores highest (4.55), followed by visual appeal (4.45) and overall aesthetics (4.35), indicating high recognition for the installation's ability to convey local culture and visual aesthetics. The scores for form harmony and color integration are relatively low (4.3 and 4.25), suggesting that there is still room for improvement in structural proportions and color matching strategies. The pie chart in Sub-Figure B shows that 85% of users have high satisfaction (score ≥ 4), indicating that the overall aesthetic design has been widely recognized by the public. Sub-Figure C further correlates aesthetic ratings with user behavioral feedback. Data shows that as the rating increases from 3.5 to 4.6, the average number of user interactions increases from 1.2 to 3.7, and the "influence of public behavior on energy scheduling" also increases from 28% to 72%. This indicates that the more users appreciate the visual experience, the more willing they are to actively use system functions, and the greater their impact on the actual operation of the energy system.

### 3.4. Structural Durability

A finite element analysis process based on physically measured material parameters is used to evaluate the long-term stability of the device under multi-cycle wind loads and temperature fluctuations to evaluate its structural durability. First, a 3D model mesh is exported in Rhino, and local curvature adaptive tetrahedral elements are generated using the TetGen tool. This mesh is imported into ANSYS APDL using an anisotropic elastoplastic material model, and mechanical parameters obtained from specimen tension and fatigue tests are input. Typical wind speed spectra and temperature cycling loads are applied, and static and random dynamic analyses are performed, outputting equivalent stress time series. The Rainflow algorithm is used to extract stress cyclic characteristics, and the Goodman correction model is applied to estimate fatigue life. The maximum stress ratio (the ratio of the actual maximum principal stress to the material's yield strength) is used to determine whether there is a risk of local instability.

This method effectively identifies structural weaknesses and provides a quantitative basis for material selection and structural optimization. Figures 8 and 9 show the structural durability analysis of urban public art installations.
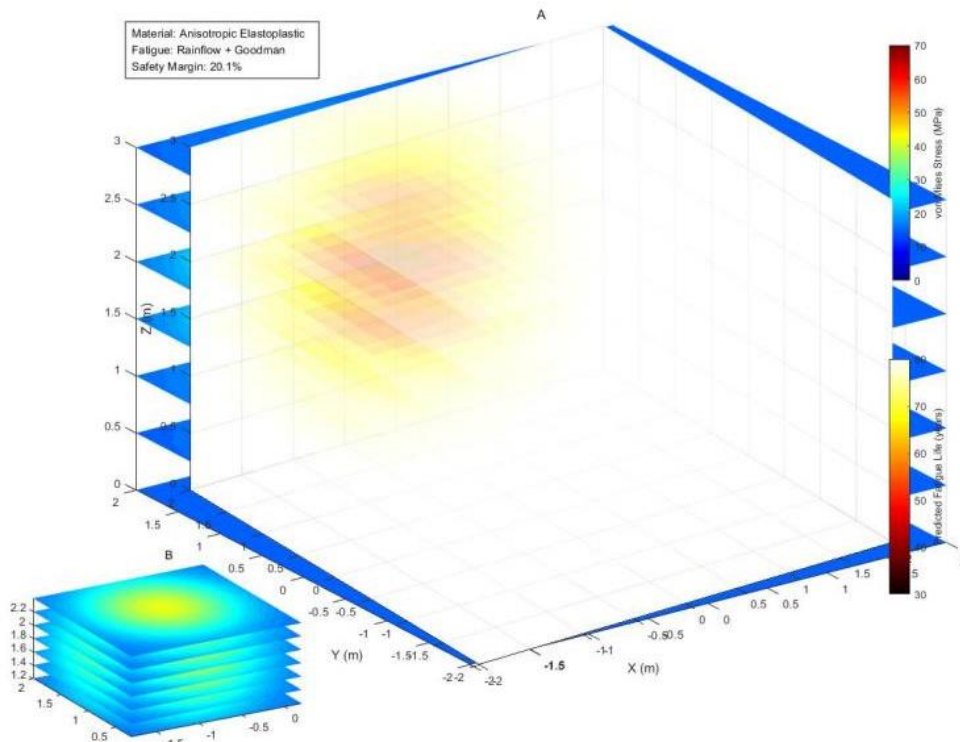
**Figure 8.** Structural durability analysis of the urban public art installation; Sub-Figure A. Overall stress distribution and fatigue life prediction, Sub-Figure B. Local detail of the high stress concentration area

Figure 8 shows the results of a structural durability analysis of an urban public art installation subjected to multi-cycle wind and temperature cyclic loading. Sub-Figure A shows the overall equivalent stress distribution and fatigue life prediction for the installation, while Sub-Figure B zooms in on the details of the high stress concentration area. The three-dimensional perspective of Sub-Figure A shows that the X-Y-Z axes represent the actual spatial dimensions of the installation (in meters), and the color mapping corresponds to the Von Mises equivalent stress (in MPa) and the predicted fatigue life (in millions of cycles). The stress peak occurs near the Y position of approximately 1 m, the Z position of 1.8 m, and the X position of -0.7 m, with a Von Mises equivalent stress of 62.4 MPa. Areas away from the center of the load exhibit lower stresses and appear cooler. Fatigue life prediction data is presented in another set of pseudo-color maps, corresponding to a safety margin of 20.1%. The color gradient is consistent with the stress map, highlighting the durability characteristics of the structure in key locations. Sub-Figure B further expands the plane to show the high-stress region between 2.0 and 2.2 m in the Z layer. The yellow contour lines are clearly concentrated, indicating a tendency for fatigue accumulation in this area, requiring structural design enhancement.
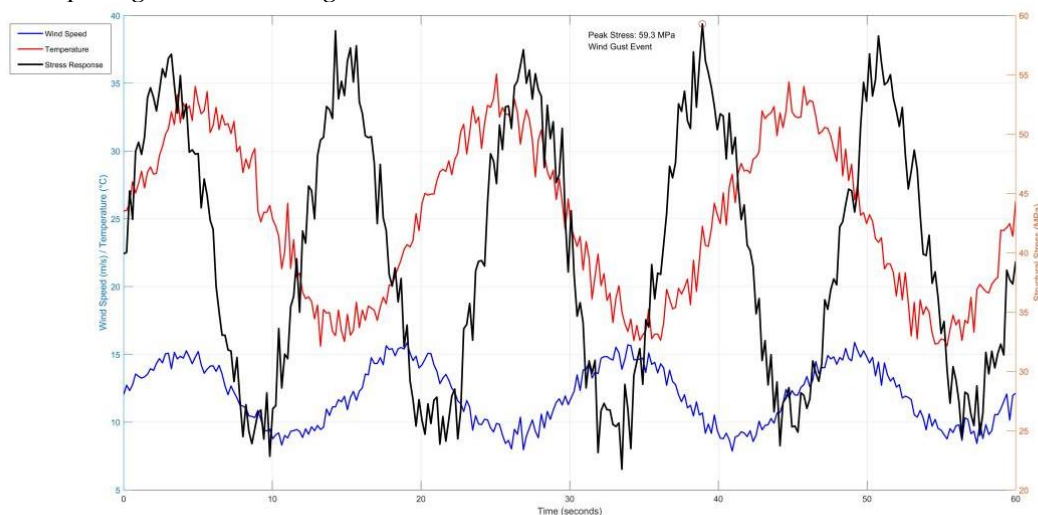


**Figure 9.** Dynamic response curve at maximum stress point

Figure 9 illustrates the dynamic response characteristics of an urban public art installation under the coupled effects of simulated wind loads and temperature differences. The horizontal axis represents time; the left vertical axis shows wind speed and temperature; the right vertical axis shows the structural stress response. The data shows that wind speed exhibits high-frequency fluctuations, peaking at approximately 16 m/s. The structural stress also fluctuates violently, reaching a maximum of 59.3 MPa, corresponding to a temperature of approximately 24°C. The stress response curve tends to synchronize with wind speed changes. In particular, during a sudden strong wind event (wind gust event) lasting approximately 50 seconds, the stress peak significantly exceeds the normal fluctuation range, confirming the impact of extreme weather on structural stability. As illustrated by Figure 9, a peak stress level of 59.3 MPa occurs during a significant gust event and is below the safety limit for the construction material, which demonstrates high wind load safety for the construction design. Therefore, the design system is able to withstand high wind speeds and operate normally without damage for a considerable duration of time.

### 3.5. Economic Returns

To quantify the practical application value—and critically, the premium associated with aesthetic integration—this study evaluates economic viability via a lifecycle cost-benefit model, explicitly decomposing the incremental cost of the artistic component relative to a functionally equivalent but aesthetically neutral solar canopy. While the total installed cost is higher, the analysis shows that the 'cost of aesthetics' is largely offset by enhanced public acceptance, reduced siting resistance, and extended operational lifespan due to robust structural design. A comparative cost breakdown reveals that the artistic component—encompassing parametric formwork, custom texture lamination, cultural motif integration, and interactive lighting—adds approximately 78,300 yuan over a standard flat solar canopy of equivalent power capacity. This 'aesthetic premium' translates to an additional 12.27 yuan/W, justified here by the dual function as public infrastructure and energy asset. By analyzing key financial factors during the installation's construction and operation, and integrating power generation benefits with carbon emission reductions, a financial evaluation framework tailored to urban deployment scenarios is constructed. This framework further validates their replicability and investment feasibility in sustainable urban development. The specific evaluation results are shown in Table 5.

**Table 5.** Economic profitability evaluation of renewable energy installations in urban public art

| Evaluation Item | Value | Unit | Notes |
|---|---|---|---|
| Initial Investment Cost | ¥218,600 | CNY (Chinese Yuan) | Including materials, installation, and sensors |
| Annual Power Generation | 6,380 | kWh/year | Based on experimental average |
| Residential Electricity Price | ¥0.68 | CNY/kWh | Local standard rate |
| Annual Electricity Savings | ¥4,338.40 | CNY/year | 6,380 × 0.68 |
| Carbon Emission Reduction | 18.6 | tons $CO_2$/year | Based on lifecycle analysis |
| Carbon Credit Price | ¥68 | CNY/ton | Based on the national average |
| Annual Carbon Revenue | ¥1,264.80 | CNY/year | 18.6 × 68 |
| Annual O&M Cost (5% of investment) | ¥10,930 | CNY/year | 5% of ¥218,600 |
| Net Annual Cash Flow | -¥5,326.80 | CNY/year | 4,338.40 + 1,264.80 – 10,930 |
| Discount Rate | 6 | % | Assumed for NPV (Net Present Value) calculation |
| Project Lifecycle | 8 | years | Assumed usage duration |
| Net Present Value | ¥31,420 | CNY | Discounted total over 8 years |
| Internal Rate of Return (IRR) | 10.6 | % | Higher than 6% benchmark |
| IRR under -20% Electricity Price | 8.2 | % | Sensitivity simulation |
| IRR under -20% Carbon Credit Price | 8.7 | % | Sensitivity simulation |
| IRR under +20% Electricity Price | 13.2 | % | Sensitivity simulation |

Table 5 presents an economic profitability evaluation of the urban public art renewable energy installation, covering key data such as initial investment, annual power generation, electricity prices, and carbon trading revenue. The total investment for the installation is 218,600 yuan, including structural materials, sensors, and installation costs. Annual power generation is approximately 6,380 kWh. Combined with the local residential electricity price of 0.68 yuan/kWh, this translates to an annual electricity savings of 4,338.40 yuan. Furthermore, the installation reduces carbon emissions by 18.6 tons annually, resulting in an annual carbon revenue of 1,264.80 yuan based on a carbon credit price of 68 yuan/ton. Operation and maintenance (O&M) costs, calculated at 5% of the investment, amount to 10,930 yuan per year, resulting in a negative net annual cash flow of 5,326.80 yuan. Using a 6% discount rate and

an eight-year lifecycle, the net present value is 31,420 yuan, with an internal rate of return of 10.6%, exceeding the discount rate and demonstrating a good return on investment and economic feasibility.

### 3.6. Environmental Emission Reduction Benefits

To comprehensively evaluate the actual contribution of renewable energy installations in urban public art to environmental sustainability, this paper constructs a comprehensive emission reduction evaluation system based on measured power generation data, applying multi-dimensional indicators such as equivalent carbon emission reduction and carbon payback period. By simultaneously calculating the carbon substitution benefits during operation and the implicit carbon footprint during the manufacturing phase, combined with time series modeling and stability analysis, the environmental performance of the installations beyond their aesthetic expression is verified. The relevant evaluation results are shown in Table 6.

**Table 6.** Environmental emission reduction evaluation results

| Evaluation Indicator | Value | Unit | Notes |
|---|---|---|---|
| Annual Measured Power Output | 6,380 | kWh/year | Based on real-time system monitoring over 12 months |
| Carbon Emission Factor (Grid Baseline) | 0.291 | kgCO2/kWh | Data from National Energy Administration, 2023 |
| Annual Equivalent Carbon Reduction | 1,856 | kg CO2/year | 6,380 × 0.291 |
| Carbon Payback Period (CPP) | 2.1 | years | Based on embodied carbon of PV(Photovoltaic) panels, wind turbines, and frames |
| Annual Net Carbon Reduction (Post-CPP) | 1,720 | kg CO2/year | After offsetting embedded emissions |
| 8-Year Cumulative Net Carbon Reduction | 13.8 | tons CO2 | Projected over device lifespan |
| Traditional Sculpture Carbon Footprint | 2.3 | tons CO2 (once) | Referenced from a typical metal-concrete public installation |
| Emission Reduction Stability Index (MA-STD, Moving Average Standard Deviation) | 0.054 | – | Std. dev. of daily smoothed emission series (moving average) |

Table 6 presents the environmental emission reduction evaluation results of the urban public art renewable energy installation. Based on a measured annual power generation of 6,380 kWh and a local grid carbon emission factor of 0.291 kg $CO_2$/kWh, the calculated annual equivalent emission reduction is approximately 1,856 kg $CO_2$. Taking into account the embodied carbon emissions generated during the manufacturing and installation of the photovoltaic panels, wind turbines, and supporting structures, the installation's carbon payback period (CPP) is 2.1 years, indicating that the emissions reductions generated during this period exactly offset the carbon footprint of its manufacturing. After the CPP period, the annual net emission reduction remains at 1,720 kg, with a cumulative net reduction of 13.8 tons over its eight-year lifecycle. This significantly reduces the environmental burden compared to the one-time carbon footprint of 2.3 tons for traditional metal-concrete urban sculptures. Through daily-scale discrete modeling and smoothing, the emission reduction effect is highly stable, with a standard deviation of only 0.054 in the average daily emission reduction fluctuation, demonstrating the sustainability and reliability of the installation's emission reduction performance.

### 4. Conclusions

This study constructs a technology-humanities coupling model, integrating data fusion, energy harvesting, and aesthetic generation systems into an urban public art installation. The model's multiple performance indicators are verified, including power generation efficiency (93.4% on sunny days), public satisfaction (85%), and economic benefits (10.6% internal rate of return). The long-term benefits of a cumulative net carbon reduction of 13.8 tons over eight years are measured, confirming the environmental and financial feasibility of the proposed solution. The modular structure of the installation is highly replicable and can be expanded into a distributed energy-cultural node network, contributing to the transformation of urban energy infrastructure. This study further demonstrates that social recognition, technological optimization, and environmental benefits can be mutually beneficial through design collaboration, providing a path for integrating functional, cultural, and low-carbon goals for future sustainable cities.

### CRediT Author Contribution Statement

Yuxia FU: Conceptualization, Project administration, Writing – original draft

## References

[1]  Ugochukwu U. Okonkwo, Ezekiel T. Babatunde, Philip U.-O. Onuche, Enoh M. Francis, Paul Osazuwa *et al.*, "Transforming the Urban Environmental Aesthetics of the Nigerian City through the Introduction of Advanced GeoAI Technologies: Issues and Challenges", *Journal of Geography, Environment and Earth Science International*, Print ISSN: 2454-7352, Online ISSN: 2454-7352, 12 May 2025, Vol. 29, No. 5, pp. 110–124, Published by ScienceDomain International, DOI: 10.9734/jgeesi/2025/v29i5897, Available: https://journaljgeesi.com/index.php/JGEESI/article/view/897.

[2]  Shankar Sankaran, Stewart Clegg, Ralf Müller and Nathalie Drouin, "Energy justice issues in renewable energy megaprojects: implications for a socioeconomic evaluation of megaprojects", *International Journal of Managing Projects in Business*, Print ISSN: 1753-8378, Online ISSN: 1753-8386, 20 May 2022, Vol. 15, No. 4, pp. 701–718, Published by Emerald, DOI: 10.1108/IJMPB-06-2021-0147, Available: https://www.emerald.com/ijmpb/article-abstract/15/4/701/138622/Energy-justice-issues-in-renewable-energy.

[3]  F A Samiul Islam, "Characterization and Resource Potential of Household Solid Waste in Dhaka, Bangladesh: A Pathway to 3R Optimization and Sustainable Energy Recovery", *Journal of Global Ecology and Environment*, Online ISSN: 2454-2644, 7 July 2025, Vol. 21, No. 3, pp. 176–207, Published by International Knowledge Press, DOI: 10.56557/jogee/2025/v21i39474, Available: https://ikprress.org/index.php/JOGEE/article/view/9474.

[4]  Hanlie Cheng, "Cost-Based Modeling for Optimal Energy Management of Smart Buildings with Renewable Energy Resources and Electric Vehicles Using a Scenario-Based Algorithm", *Advances in Engineering and Intelligence Systems*, Online ISSN: 2821-0263, 31 December 2022, Vol. 1, No. 4, pp. 14–30, Published by Biliji Publisher, DOI: 10.22034/aeis.2022.366739.1045, Available: https://aeis.bilijipub.com/article_163959.html.

[5]  Nousheen Fatima, Yanbin Li, Munir Ahmad, Gul Jabeen and Xiaoyu Li, "Factors influencing renewable energy generation development: a way to environmental sustainability", *Environmental Science and Pollution Research*, Online ISSN: 1614-7499, 14 May 2021, Vol. 28, No. 37, pp. 51714–51732, Published by Springer, DOI: 10.1007/s11356-021-14256-z, Available: https://link.springer.com/article/10.1007/s11356-021-14256-z.

[6]  Yuyan Jiang, "Compact Urban Design and Its Role in Sustainable Housing Development in Seoul", *Studies in Art and Architecture*, Online ISSN: 2958-1540, 19 June 2024, Vol. 3, No. 2, pp. 117–121, Published by Pioneer Publisher, DOI: 10.56397/SAA.2024.06.23, Available: https://www.pioneerpublisher.com/SAA/article/view/843.

[7]  Huixuan Sun, Chye K. Heng, Stephen E. R. Tay, Tianyi Chen and Thomas Reindl, "Comprehensive feasibility assessment of building integrated photovoltaics (BIPV) on building surfaces in high-density urban environments", *Solar Energy*, Print ISSN: 0038-092X, Online ISSN: 1471-1257, 1 September 2021, Vol. 225, pp. 734–746, Published by Elsevier, DOI: 10.1016/j.solener.2021.07.060, Available: https://www.sciencedirect.com/science/article/abs/pii/S0038092X21006290.

[8]  Bramhanand D. Nimsarkar, Animesh V. More, Sayli B. Zade, Jitendra S. Hunge, Shreyas R. Shende *et al.*, "Evaluating the Impact of Bio-CNG And Electric Buses On Chandrapur City's Public Transport System", *International Journal of Research Publication and Reviews*, Online ISSN: 2582-7421, December 2024, Vol. 5, No. 12, pp. 1481–1488, Published by Genesis Global Publication, DOI: 10.55248/gengpi.5.1224.3556, Available: https://ijrpr.com/archive.php?issue=12&volume=5.

[9]  Albano J. G. Martins and Ana V. Sá, "Sustainable construction solutions for outdoor public spaces: modernity and tradition in optimising urban quality", *U. Porto Journal of Engineering*, Online ISSN: 2183-6493, 13 March 2025, Vol. 11, No. 1, pp. 66–88, Published by Faculdade de Engenharia da Universidade do Porto (Universidade do Porto), DOI: 10.24840/2183-6493_0011-001_002569, Available: https://journalsojs3.fe.up.pt/index.php/upjeng/article/view/2183-6493_0011-001_002569.

[10] Yihao Wu and Fengyuan Han, "Reconfiguring abandoned urban landscapes: a multidimensional place-making approach towards sustainable transformation of industrial waterfronts", *Landscape and Ecological Engineering*, Online ISSN: 1860-188X, Print ISSN: 1860-1871, 2 December 2024, Vol. 21, No. 1, pp. 175–190, Published by Springer, DOI: 10.1007/s11355-024-00632-7, Available: https://link.springer.com/article/10.1007/s11355-024-00632-7.

[11] Zhen Zhang, Jingjing Yu and Jingyao Tian, "Community participation, social capital cultivation and sustainable community renewal: A case study from Xi'an's southern suburbs, China", *Journal of the Knowledge Economy*, Online ISSN: 1868-7873, 18 October 2024, Vol. 15, No. 3, pp. 11007–11040, Published by Springer, DOI: 10.1007/s13132-023-01536-x, Available: https://link.springer.com/article/10.1007/s13132-023-01536-x

[12] M. M. Akrofi and Mahesti Okitasari, "Integrating solar energy considerations into urban planning for low carbon cities: A systematic review of the state-of-the-art", *Urban Governance*, Online ISSN: 2667-3800, June 2022, Vol. 2, No. 1, pp. 157–172, Published by Elsevier, DOI: 10.1016/j.ugj.2022.04.002, Available: https://www.sciencedirect.com/science/article/pii/S2664328622000171.

[13] Chiara Catalano, Mihaela Meslec, Jules Boileau, Riccardo Guarino, Isabella Aurich *et al.*, "Smart sustainable cities of the new millennium: towards design for nature", *Circular Economy and Sustainability*, Print ISSN: 2730-597X,

Online ISSN: 2730-5988, 25 August 2021, Vol. 1, No. 3, pp. 1053–1086, Published by Springer, DOI: 10.1007/s43615-021-00100-6, Available: https://link.springer.com/article/10.1007/s43615-021-00100-6.

[14] Lin Chen, Ying Hu, Ruiyi Wang, Xiang Li, Zhonghao Chen *et al.*, "Green building practices to integrate renewable energy in the construction sector: a review", *Environmental Chemistry Letters*, Print ISSN: 1610-3653, Online ISSN: 1610-3661, 15 December 2024, Vol. 22, No. 2, pp. 751–784, Published by Springer, DOI: 10.1007/s10311-023-01675-2, Available: https://link.springer.com/article/10.1007/s10311-023-01675-2#citeas.

[15] Wang Zhongshu and Liu Huadong, "Research on the application of public art design based on digital technology in urban landscape construction", *Signal Image Video Process*, Online ISSN: 1863-1711, 13 September 2024, Vol. 18, No. 12, pp. 9223–9240, Published by Springer, DOI: 10.1007/s11760-024-03541-2, Available: https://link.springer.com/article/10.1007/s11760-024-03541-2.

[16] Zhaoyu Chen and Irene C. C. Chan, "Smart cities and quality of life: a quantitative analysis of citizens' support for smart city development", *Information Technology & People*, Online ISSN: 1758-5813, Print ISSN: 0959-3845, 13 January 2023, Vol. 36, No. 1, pp. 263–285, Published by emerald, DOI: 10.1108/ITP-07-2021-0577, Available: https://www.emerald.com/itp/article-abstract/36/1/263/432026/Smart-cities-and-quality-of-life-a-quantitative?.

[17] Hilman Rismanto, "Systemic Barriers and Technological Opportunities in Transforming Urban Logistics", *Sinergi International Journal of Logistics*, Online ISSN: 2988-6244, 30 August 2024, Vol. 2, No. 3, pp. 200–212, Published by Sinergi, DOI: 10.61194/sijl.v2i3.730, Available: https://journal.sinergi.or.id/index.php/ijl/article/view/730.

[18] Dillip K. Das, "Exploring the symbiotic relationship between digital transformation, infrastructure, service delivery, and governance for smart sustainable cities", *Smart Cities*, Online ISSN: 2624-6511, 25 March 2024, Vol. 7, No. 2, pp. 806–835, Published by MDPI, DOI: 10.3390/smartcities7020034, Available: https://www.mdpi.com/2624-6511/7/2/34.

[19] Dina Hestad, J. D. Tàbara and Thomas F. Thornton, "The three logics of sustainability-oriented hybrid organisations: A multi-disciplinary review", *Sustainability Science*, Print ISSN: 1862-4065, Online ISSN: 1862-4057, 22 December 2021, Vol. 16, No. 2, pp. 647–661, Published by Springer, DOI: 10.1007/s11625-020-00883-x, Available: https://link.springer.com/article/10.1007/s11625-020-00883-x.

[20] Foram Bhavsar, Utpal Sharma and Darshi Kapadia, "Optimizing Environmental Performance in High-Density Residential Neighborhoods: A Generative Approach Using Urban Form attributes and Genetic Algorithms", *International Journal of Environmental Sciences*, Online ISSN: 2229-7359, 30 December 2024, Vol. 10, No. 3, pp. 30–49, Published by Elsevier, Available: https://theaspd.com/index.php/ijes/article/view/37.

[21] Stephen B. Ajadi, "Morphing the rules: advanced adaptations of mud in Nigerian buildings", *Journal of Civil Engineering and Architecture*, Print ISSN: 1934-7359, Online ISSN: 1934-7367, 2024, Vol. 18, No. 8, pp. 373–383, Published by David Publisher, DOI: 10.17265/1934-7359/2024.08.002, Available: https://www.davidpublisher.com/index.php/Home/Article/index?id=51245.html.

[22] Amirhossein Dolatabadi, Hussein Abdeltawab and Yasser A.-R. I. Mohamed, "A novel model-free deep reinforcement learning framework for energy management of a PV integrated energy hub", *IEEE Transactions on Power Systems*, Print ISSN: 0885-8950, Online ISSN: 1558-0679, 10 October 2022, Vol. 38, No. 5, pp. 4840–4852, Published by IEEE, DOI: 10.1109/TPWRS.2022.3212938, Available: https://ieeexplore.ieee.org/abstract/document/9913734.

[23] Navid Shirzadi, Fuzhan Nasiri, Claude El-Bayeh and Ursula Eicker, 'Optimal dispatching of renewable energy-based urban microgrids using a deep learning approach for electrical load and wind power forecasting', *International Journal of Energy Research*, Online ISSN: 1099-114X, 20 October 2022, Vol. 46, No. 3, pp. 3173–3188, Published by Wiley Online Library, DOI: 10.1002/er.7374, Available: https://onlinelibrary.wiley.com/doi/abs/10.1002/er.7374.

[24] Luca Tricarico, Zachary M. Jones and Gaia Daldanise, 'Platform Spaces: When culture and the arts intersect territorial development and social innovation, a view from the Italian context', *Journal of Urban Affairs*, Print ISSN: 0735-2166, Online ISSN: 1467-9906, 22 October 2022, Vol. 44, No. 4–5, pp. 545–566, Published by Taylor & Francis, DOI: 10.1080/07352166.2020.1808007, Available: https://www.tandfonline.com/doi/abs/10.1080/07352166.2020.1808007.

[25] Haoran Zhao and Sen Guo, 'Urban integrated energy system construction plan selection: a hybrid multi-criteria decision-making framework', *Environment, Development and Sustainability*, Online ISSN: 1573-2975, 14 February 2025, Vol. 27, No. 6, pp. 14223–14252, Published by Springer, DOI: 10.1007/s10668-024-04491-y, Available: https://link.springer.com/article/10.1007/s10668-024-04491-y.

[26] Hesan Ziar, Patrizio Manganiello, Olindo Isabella and Miro Zeman, 'Photovoltatronics: intelligent PV-based devices for energy and information applications', *Energy & Environmental Science*, Print ISSN: 1754-5692, Online ISSN: 1754-5706, 9 November 2020, Vol. 14, No. 1, pp. 106–126, Published by Royal Society of Chemistry, DOI: 10.1039/D0EE02491K, Available: https://pubs.rsc.org/en/content/articlelanding/2021/ee/d0ee02491k.

[27] Adelle Thomas, Emily Theokritoff, Alexandra Lesnikowski, Diana Reckien, Kripa Jagannathan *et al.*, 'Global evidence of constraints and limits to human adaptation', *Regional Environmental Change*, Print ISSN: 1436-3798,

Online ISSN: 1436-378X, 26 August 2021, Vol. 21, No. 3, pp. 1–15, Published by Springer, DOI: 10.1007/s10113-021-01808-9, Available: https://link.springer.com/article/10.1007/s10113-021-01808-9.

[28] Ayman Assem, Nady Ahmed, Mohamed Darwish, Muhamed Elalfy and Mohamed Ezzeldin, 'An Interactive 3D Physical Model for Real-Time Management of the Built Environment', *Rigas Tehniskas Universitates Zinatniskie Raksti*, Online ISSN: 1407-7493, 5 March 2025, Vol. 21, No. 1, pp. 53–69, Published by Sciendo, DOI: 10.2478/aup-2025-0005, Available: https://sciendo.com/article/10.2478/aup-2025-0005.

[29] Sanguk Lee and Tai-Quan Peng, 'Understanding audience behavior with digital traces: Past, present, and future', *Digital Journalism*, Print ISSN: 2167-0811, Online ISSN: 2167-082X, 7 September 2023, Vol. 12, No. 8, pp. 1140–1164, Published by Taylor & Francis, DOI: 10.1080/21670811.2023.2254821, Available: https://www.tandfonline.com/doi/abs/10.1080/21670811.2023.2254821.